

Suppressed migrating diurnal tides in the MLT region during El Niño in Northern Winter and its possible mechanism

**Yetao Cen^{1,2,3}, Chengyun Yang^{1,2,3*}, Tao Li^{1,2,3*}, Jia Yue^{5,6}, James M. Russell III⁶,
and Xiankang Dou^{1,2,3,4}**

¹CAS Key Laboratory of Geospace Environment, School of Earth and Space Sciences,
University of Science and Technology of China, Hefei, Anhui, China

²Mengcheng National Geophysical Observatory, School of Earth and Space Sciences,
University of Science and Technology of China, Hefei, Anhui, China

³CAS Center for Excellence in Comparative Planetology, University of Science and
Technology of China, Hefei, Anhui, China

⁴School of Electronic Information, Wuhan University, Wuhan, Hubei, China

⁵Catholic University of America, DC, USA

⁶Center for Atmospheric Sciences, Hampton University, Hampton, VA, USA

Correspondence: Chengyun Yang (cyang@ustc.edu.cn) and Tao Li
(litao@ustc.edu.cn)

Abstract

As observed by the Sounding of the Atmosphere using Broadband Emission Radiometry (SABER), the migrating diurnal tide (DW1) in the upper mesosphere and lower thermosphere (MLT) region decreased by ~10% during El Niño in the Northern Hemisphere (NH) winter (December-January-February) from 2002 to 2020. According to the multiple linear regression (MLR) analysis, the linear effects of El Niño on the tropical MLT DW1 are significantly negative in both SABER observations and SD-WACCM (the Specified-Dynamics version of the Whole Atmosphere Community Climate Model) simulations. The DW1 response to El Niño in NH winter is much stronger than its annual mean response. As suggested by SD-WACCM simulation, Hough mode (1, 1) dominates the DW1 tidal variation in the tropical MLT region. The consistency between the (1, 1) mode in the tropopause region and the MLT region and the downward phase progression from 15 to 100 km indicates the direct upward propagation of DW1 from the excitation source in the troposphere. The suppressed DW1 heating rates in the tropical troposphere (averaged over ~0-16 km and 35°S-35°N) during El Niño winter contribute to the decreased DW1 tide. To evaluate the effect of the gravity waves (GW) on the tide, the GW forcing is calculated as the GW drag weighted by the phase relation between DW1 GW drag and DW1 wind. The negative GW forcing in the tropical upper mesosphere would significantly suppress the MLT DW1 tide during El Niño winter. This tidal-GW interaction could be a dominant mechanism for DW1 response in the MLT to El Niño. During El Niño winter, the increased ratio of the absolute and planetary vorticity (R) suppresses the waveguide and thus the DW1 amplitude in the subtropical mesosphere. However, the effect of the waveguide might play a secondary role due to its relatively weak response.

删除[cyt]: SABER (

删除[cyt]: the

删除[cyt]: average

删除[cyt]: the

删除[cyt]: events

删除[cyt]: tidal

删除[cyt]: in the MLT region

删除[cyt]: <sp>

1 Introduction

Atmospheric solar tides are global-scale variations in meteorological variables (e.g., density, wind, and temperature) with subharmonic periods of a solar day. The migrating diurnal tide is dominant in the tropical mesosphere and lower thermosphere (MLT) region and is characterized by westward traveling zonal wavenumber 1, denoted as DW1 (Chapman & Lindzen, 1970). DW1 is primarily excited by the absorption of infrared (IR) radiation by water vapor in the troposphere (~0–15 km) (Hagan et al., 2002) and can propagate vertically and reach maximum amplitude in the MLT region (Walterscheid., 1981a; McLandress et al., 1996; Liu & Hagan, 1998; Lu et al., 2009; Liu et al., 2010; Yang et al., 2018). Diurnal migrating tides remain a significant focus of scientific research due to a lack of comprehensive understanding of their seasonal and interannual variabilities. The tidal variation in the MLT region depends on variations in the wave sources, such as the solar heating absorption in the lower atmosphere (Chapman & Lindzen, 1970), and the tidal wave propagation, which is affected by background wind variation, such as the QBO (Forbes and Vincent, 1989; Hagan et al., 1999; McLandress, 2002a; Ramesh et al., 2020; McLandress, 2002b; Mayr and Mengel, 2005). In addition to tidal sources and propagation, tidal variability is also affected by the modulation of interactions with gravity waves (GW) (Liu and Hagan, 1998; Li et al., 2009).

As the dominant interannual variation in the tropical troposphere (Yulaeva and Wallace, 1994), the El Niño-Southern Oscillation (ENSO), which is characterized by anomalous sea surface temperature in the eastern equatorial Pacific Ocean, can cause global-scale perturbations in atmospheric temperature, rainfall, and cloudiness and potentially modulate tidal heating sources in the troposphere (Lieberman et al., 2007). Previous studies have documented that ENSO can influence the troposphere (Yulaeva and Wallace, 1994; Calvo-Fernandez et al., 2004) and the stratosphere and mesosphere (Sassi et al., 2004; Randel et al., 2009; Li et al., 2013 and 2016). ENSO events tend to reach their maximum in the Northern Hemisphere (NH) winter; they could significantly impact the MLT tide.

删除[cyt]: <sp>

According to meridional wind observations from the meteor radar at Jakarta (6.4°S, 106.7°E) and medium-frequency (MF) radar at Tirunelveli (8.7°N, 77.8°E), the tropical diurnal amplitudes in the meridional winds were suppressed during the El Niño winters of 1994/1995 and 1997/1998 (Gurubaran et al., 2005). However, Lieberman et al. (2007) documented a dramatic enhancement of the subtropical diurnal tide in 1997 based on MF radar observations at Kauai, Hawaii (22°N, 154°W), which may be connected to more substantial solar heating absorbed by water vapor during the strong El Niño event of 1997-1998. Notably, the diurnal tidal amplitude was only slightly enhanced during the winter of 1997/1998, when El Niño reached its maximum. However, the diurnal tidal amplitudes were suppressed during the winters of another 3 El Niño events (1991/1992, 1994/1995, and 2002/2003). Based on the observations from ground-based radars and the Sounding of the Atmosphere using Broadband Emission Radiometry (SABER) onboard the Thermosphere Ionosphere Mesosphere Energetics and Dynamics (TIMED) satellite, Vitharana et al. (2021) documented that the DW1 response to El Niño was negative from 2003 to 2016, considering all the months. However, the response of DW1 to ENSO is different or even opposite in different seasons, as suggested by previous studies (e.g., Lieberman et al., 2007; Zhou et al., 2018; Kogure et al., 2021). For instance, Lieberman et al. (2007) reported a dramatic enhancement of the subtropical diurnal tide during the 1997 autumn based on MF radar. From July to October of the strong El Niño of 2015, the equatorial DW1 in the MLT was also dramatically enhanced in SABER (Zhou et al., 2018; Kogure et al., 2021). Thus, calculating the regression by binning the data among different months together may underestimate the actual response of MLT DW1 tide in a particular season. Since ENSO reaches its peak in winter, more pronounced effects in the upper atmosphere are expected. Thus, we focus on the linear response of DW1 to ENSO during the winter in this study.

删除[cyt]:)/SABER

删除[cyt]: equatorial

Utilizing the Whole Atmosphere Community Climate Model (WACCM) version 4, Pedatella & Liu (2012 and 2013) suggested that El Niño could enhance the MLT DW1 tide during winters due to increased tropospheric radiative forcing. The QBO

删除[cyt]: In their simulation, the

删除[cyt]: <sp>

signal is prescribed in WACCM4, and the ENSO events are self-generated. Based on the WACCM version 6 simulations in which the QBO and ENSO are self-generated, Ramesh et al. (2020) investigated the linear response of latitude-pressure variation of DW1-T to the seven predictors, including ENSO in four seasons by adopting the Multivariate linear regression. As suggested in Figure 5 by Ramesh et al. (2020), the linear response of DW1 T amplitude to ENSO is significantly positive during the NH winter in the tropical MLT region. However, Liu et al. (2017) found that DW1 amplitudes are suppressed during the winters of El Niño events based on simulations of the ground-to-topside atmosphere-ionosphere for aeronomy (GAIA) model. Since GAIA is nudged with reanalysis data below 30 km, ENSO events and variations in the lower atmosphere are more realistic. The discrepancies among the model simulations and uncertainties in the observations require further investigation of the DW1 tide-ENSO connection.

删除[cyt]: not included

删除[cyt]: During the NH winter, as

删除[cyt]: by

删除[cyt]: in

The response of the MLT DW1 tide to ENSO during the winters is revisited in this study based on the DW1 variation extracted from a long-term temperature dataset observed by the SABER onboard the TIMED satellite (Mertens et al., 2001, & 2004; Rezac et al., 2015). The “Specified-Dynamics” version of the WACCM simulation is used to study the possible mechanism. The data and methods are described in section 2. Section 3 presents the observational and model results of the DW1 temperature response to ENSO. Section 4 examines the possible mechanism that modulates the MLT DW1 tide during ENSO events. Finally, a summary is presented in section 5.

删除[cyt]: Sounding of the Atmosphere using Broadband Emission Radiometry (

删除[cyt]:)

删除[cyt]: ,

删除[cyt]: ,

删除[cyt]: .

2 Data and Methods

The SABER began its observations in January 2002. Kinetic temperature profiles are retrieved from the CO2 limb emission profiles from the tropopause to the lower thermosphere using a full non-LTE inversion (Mertens et al., 2001, 2004, Rezac et al. 2015). The latitude range of SABER observations is from 53° in one hemisphere to 83° in the other, and the latitude coverage flips to the opposite hemisphere

删除[cyt]: Onboard the TIMED satellite,

删除[cyt]: <sp>

approximately every 60 days. Thus, SABER provides nearly continuous soundings within 53°S and 53°N. This study used version 2.0 temperature data from February 2002 through July 2021 to analyze the DW1 temperature tide in the MLT region. SABER can complete a nearly 24-hr local time observation within a ~60-day window, allowing us to extract the diurnal tide explicitly.

The method described by Xu et al. (2007) is utilized to extract the DW1 tide from TIMED/SABER temperature data. Migrating tides can be expressed as

$$\frac{1}{2\pi} \int_0^{2\pi} T(t_{LT}, \lambda) d\lambda = T(t_{LT}) + \sum_{n=1}^N T_n^{mtw} \cos(n\omega_0 \pm \psi_n^{mtw}) + \varepsilon \quad (1)$$

where T is temperature, t_{LT} is local time, λ is longitude, $\overline{}$ denotes zonal mean, the second term on the right side $\sum_{n=1}^N T_n^{mtw} \cos(n\omega_0 \pm \psi_n^{mtw})$ refers to migrating tides with $n = 1, 2, 3, 4$ corresponding to the diurnal, semidiurnal, terdiurnal and 6-h periods, T_n^{mtw} and ψ_n^{mtw} are the amplitude and phase of the migrating tide, and ε is the remnant of the temperature variability which could not be represented by the first two terms. The daily data are first divided into two groups according to their local time corresponding to the ascending and descending phases, respectively, to extract tidal components. Then, each group is interpolated into 12 longitude grids, each 30° wide, by fitting with a cubic spline. The next step is to calculate the zonal mean for each day to eliminate the nonmigrating tides and the stationary planetary waves. The migrating tides' bimonthly amplitudes and phase information can be calculated by nonlinear least-squares fitting techniques using data within a 60-day sliding window every month (Xu et al., 2007; Smith et al., 2012; Gan et al., 2014).

The WACCM is a fully coupled chemistry-climate model, the high-top atmosphere component of the Community Earth System Model (CESM) (Garcia et al., 2007). In this study, the simulation of the Specified-Dynamics (SD) version of WACCM (SD-WACCM), version 4, is adopted to investigate the ENSO-DW1 tide relationship. The vertical range of SD-WACCM extends from the surface up to ~140 km. The simulated diurnal tide in WACCM4 compares favorably with observations (Lu et al., 2011; Davis et al., 2013). SD-WACCM is nudged to meteorological fields

删除[cyt]:

删除[cyt]: <math>

删除[cyt]: t_{LT}

设置格式[cyt]: 图案: 清除(白色)

删除[cyt]: <math> is

删除[cyt]: temperature, $\sum_{n=1}^N T_n^{mtw} \cos(n\omega_0 + \psi_n^{mtw})$ is

删除[cyt]: ,

设置格式[cyt]: 图案: 清除(白色)

删除[cyt]: T_{r1} is

删除[cyt]: <sp>

from Modern-Era Retrospective Analysis for Research and Applications (MERRA) reanalysis data in the troposphere and stratosphere (from the surface up to 1 hPa) and then is freely run in the MLT (above 0.3 hPa) (Kunz et al., 2011). Smith et al. (2017) discussed the dynamic constraints in SD-WACCM and their impact on the simulation of the mesosphere in detail. The ENSO-related characteristics in the troposphere and stratosphere in SD-WACCM follow those in the reanalysis meteorological fields with relaxation. In this study, the SD-WACCM output includes complete diurnal tidal information for temperature, zonal and meridional wind, and heating processes from 1979 to 2014. The simulation also outputs the diurnal components of parameterized GW drag. We note here that the WACCM version 6 simulation was not used in this study due to its opposite response of MLT DW1 to ENSO compared to SABER observations.

The Niño3.4 index (N3.4), which is the sea surface temperature (SST) anomaly, averaged over 120°-170°W and 5°S-5°N (available at https://www.esrl.noaa.gov/psd/gcos_wgsp/Timeseries/Data/Niño34), is used to identify El Niño and La Niña events.

The monthly DW1 can be specified through its amplitude and phase. To evaluate the variations in both the amplitude and phase of the DW1 tide, the monthly DW1 amplitudes are weighted by projecting the monthly mean vectors onto the climatological mean DW1 vector with the phase difference $\cos(\Delta\phi)$ (the phase difference is $\Delta\phi = \phi - \phi_{\text{clim}}$) as follows:

$$\text{Amp}_{\text{weighted}} = \text{Amp} * \cos(\omega * (\phi - \phi_{\text{clim}})) \quad (2)$$

where ω ($\omega = 2\pi/24$) is the frequency of the DW1 tide. ϕ and ϕ_{clim} are the DW1 phase of each month and the climatological mean, respectively. In the remainder of this study, the weighted DW1 amplitude (and its anomaly) refer to the DW1 amplitude (anomaly) for conciseness. The mean tidal amplitude and phase during NH winter are derived from each year's averaged tidal vectors for December, January, and

删除[cyt]: used as a vector with the ratio as the

删除[cyt]: the angle as the

删除[cyt]: <sp>

February (DJF).

To derive the winter interannual variability that may be related to ENSO, we first calculate the DW1 anomalies by removing the climatological mean seasonal cycle. Then, the winter (DJF) mean of the DW1 anomalies is calculated. Natural forcing, such as the solar cycle (represented by F107), QBO, ENSO, and long-term trends, jointly affect the DW1 tidal amplitude (e.g., Dhadly et al., 2018; Gurubaran et al., 2005; Gurubaran & Rajaram, 1999; Hagan et al., 1999; Lieberman et al., 2007; Liu et al., 2017; Pedatella & Liu, 2012; Sridharan, 2019, 2020; Sridharan et al., 2010; Vincent et al., 1998; Xu et al., 2009). To isolate the linear forcing of ENSO from the interference of other factors, a multivariate linear regression (MLR) analysis is applied to the anomalous time series at each latitude and altitude, the same as that used in Li et al. (2013).

$$T(t) = C_1 * \text{Niño3.4} + C_2 * \text{QBO10} + C_3 * \text{QBO30} + C_4 * \text{F107} + C_5 * \text{TREND} + \varepsilon(t) \quad (3)$$

where T is the DW1-T anomaly, t is time, C1–C5 are regression coefficients, and ε is the residual; QBO10 and QBO30 are two orthogonal QBO time series derived from the zonal wind (m s^{-1}) averaged over 5°N to 5°S at 10 and 30 hPa (Wallace et al., 1993), respectively. The Niño3.4 index (Niño3.4) is the 3-month running mean of SST averaged over 5°N to 5°S, 120°W–170°W; F107 is the solar radio flux at 10.7 cm, which is a proxy for solar activity; and TREND is the long-term linear trend. The linear contribution of each factor during winters is determined by applying MLR to DJF anomalies each year. The analysis is carried out from 2002 to 2020 at each latitude and pressure grid point. The F test (Kissell et al., 2017) was used to evaluate the statistical significance of the regression coefficients.

The Hough function in classic tidal theory (Chapman & Lindzen, 1970), which represents the solution of the Laplace tide equation in the isothermal atmosphere, can set a consistent latitude variation in the amplitude and phase of the tidal perturbation field. The Hough functions of daily variation frequency form a completely orthogonal set and extend from 90°S to 90°N. This estimating amplitude and phase method is based on fitting the Hough mode to the zonal structure representation and the simple

删除[cyt]: <sp>

harmonic function (sine and cosine) to the local time-varying representation. The Hough mode is represented as $\Theta_{s,n}(\theta)$, or (s, n), where s indicates the zonal wavenumber and index n is positive for gravitational modes (propagating modes) and negative for rotational modes (trapped modes). The normalized functions satisfy the following relation.

$$\int_{-90^{\circ}}^{90^{\circ}} \Theta_{1,n}(\theta) \bullet \Theta_{1,m}(\theta) \cos(\theta) d\theta = \begin{cases} 1, m = n \\ 0, m \neq n \end{cases}, n, m = \pm 1, \pm 2, \dots \quad (4)$$

$$\int_{-90^{\circ}}^{90^{\circ}} \Theta_{1,n}(\theta) \bullet \Theta_{1,m}(\theta) \cos(\theta) d\theta = \begin{cases} 1, m = n \\ 0, m \neq n \end{cases}$$

删除[cyt]:

3 Results

As presented in Figure 1a, the NH winter (December-January-February, DJF) mean amplitude of DW1 in temperature extracted from TIMED/SABER observation is the largest (~12 K) in the equatorial mesopause region from 2002 to 2013. Although the amplitude is smaller, the distribution of the DW1 T amplitude in SD-WACCM simulation (Figure 1b) is similar to that derived from SABER observation, with the maximum at 90-100 km above the equator. There are some differences between SABER and SD-WACCM: SABER has a weaker peak above the equator at 70-80 km, but this peak cannot be seen in SD-WACCM.

Figures 2a and 2b show the monthly mean DW1 temperature amplitude anomalies (removing the climatological mean seasonal cycle) averaged over 10°S-10°N at 100 km derived from SABER observations and SD-WACCM simulations between 2002 and 2020, respectively. Among the analyzed period, there were 4 El Niño events in 2002, 2006, 2009, and 2015, which are indicated with red arrows and defined by the Niño3.4 index in Figure 2c; the 3 La Niña events in 2007, 2010, and 2020 are marked with blue arrows. The anomalous DW1 amplitudes are negative during 4 El Niño winters and positive during all 3 La Niña events. The DW1 anomalies reach a positive maximum from July to October during the 2015/2016 strong El Niño event, which agrees with Zhou et al. (2018); however, they become negative in winter. When SD-WACCM and SABER overlap (2002-2014), the

删除[cyt]: <sp>

241 simulated DW1 amplitude anomalies in SD-WACCM are negative during all 3 El
242 Niño winters (2002, 2006, and 2009) and positive during 2 La Niña events. The
243 negative response of the MLT DW1 tide to El Niño in the SD-WACCM simulation
244 agrees well with that in the SABER observation.

245 In the 35-yr SD-WACCM simulations (1979-2014), the anomalous DW1
246 amplitudes averaged over 10°S-10°N at 100 km are negative during 7 of 8 El Niño
247 winters (1982, 1986, 1991, 1997, 2002, 2006, and 2009), as shown in Table 1. The
248 MLR coefficients of DW1 to normalized Niño3.4 are significantly negative in both
249 the SABER observation and SD-WACCM simulation, as shown in Figure 3. The
250 amplitude of DW1 in the equatorial region is reduced considerably. However, the
251 phase anomaly does not vary much (less than 1 hour) during El Niño winter. (Figures
252 S1, S2).

删除[cyt]: is

删除[cyt]: drifted

253 The MLT DW1 response to El Niño in winter is five times stronger than the
254 average response in SABER observations derived by Vitharana et al. (2021). This is
255 because the DW1 enhancement in El Niño autumn (e.g., Lieberman et al., 2007; Zhou
256 et al., 2018; Kogure et al., 2021) may weaken the negative response to ENSO. In the
257 simulations of Ramesh et al. (2020), different seasons also exhibit different responses
258 of DW1 to ENSO. The MLR coefficients of tropical DW1 to Niño3.4 in the SABER
259 observation (with a minimum of ~ -1 K/index) are twice as strong as those (with a
260 minimum of ~ -0.5 K/index) in the SD-WACCM simulation since the magnitude of
261 the DW1 tide is underestimated in the WACCM4 simulation (Liu et al., 2010; Lu et
262 al., 2012). The negative response of the MLT DW1-T amplitude to El Niño is
263 consistent with early MF radar/meteor radar observations and GAIA model
264 simulations with a nudging process (Gurubaran, 2005; Liu et al., 2017) but opposite to
265 free-run WACCM simulations (Pedatella & Liu, 2012 and 2013).

删除[cyt]: In winter, the

266 The MLR coefficients of the DW1 response to normalized QBO10 and QBO30
267 in the equatorial mesopause region are significantly positive, with a minimum of ~ 1
268 K/(m*s⁻¹) near 100 km (Figure S3), consistent with previous studies (Ramesh et al.

删除[cyt]: <sp>

2020). The linear effects of the QBO on the MLT DW1 tides are comparable to those of ENSO (the variances in the DW1 tide explained by ENSO, QBO10, and QBO30 are 23%, 20%, and 17%, respectively). The interaction between the QBO and ENSO may potentially modulate the ENSO-DW1 tide relationship (Gray, 1984). In this study, we focused on the linear effect of ENSO on the MLT DW1 tidal variability and the associated mechanism. In SD-WACCM, the linear regression coefficients of DW1 are a negative response to Niño3.4 and a positive response to QBO10 and QBO30, which is consistent with the SABER observation. However, the absolute value of the coefficients decreases more than that of SABER. The variance percentages of F107 are negligible compared with these three variables. In the remainder of this study, only the linear effect of ENSO on the MLT DW1 tide is discussed.

4 Possible Mechanisms

4.1 Tidal forcing and propagation

A specific tidal component, such as DW1, can be decomposed into a series of gravity wave-like modes and Rossby wave-like modes based on the Hough functions (Figure S4) (Auclair-Desrotour et al., 2017; Chapman & Lindzen, 1970; Forbes, 1995). In a qualitative sense, the tidal response can be considered a combination of GWs restored by stable stratification and inertial Rossby waves due to Coriolis acceleration. The Hough modes of the DW1 tide in the SD-WACCM simulation are analyzed to examine the mechanism of tropical DW1 tidal variation. As shown in Figure 4a, the anomalies of the DW1 temperature amplitude averaged over 10°S-10°N at 100 km are consistent with its Hough (1,1) component (the correlation coefficient between MLT DW1-T anomalies and its Hough (1,1) component is 0.99) during the NH winter from 1979 to 2013. The DW1-T amplitude anomalies and their Hough (1,1) component during El Niño years decrease by 15% compared to the climatological mean amplitude. During winters (DJF) from 1979 to 2013, the average phase of

删除[cyt]: <sp>

DW1-T over 10°S-10°N shows general downward phase progression with the height from the MLT region to the tropopause region (approximately 15 km), implying an upward group velocity for the vertically propagating gravity wave model. By tracking the downward phase progressive line, the altitude of the excitation source is estimated to be below 15 km. The DW1-T phase during El Niño winters corresponds with the climatological mean phase structure, implying that ENSO-induced tidal perturbation in the troposphere could directly propagate vertically into the MLT region. The anomalous Hough (1,1) mode of the DW1 temperature amplitude at MLT (100 km) is significantly correlated (the correlation coefficient is 0.81) with that at the tropopause region (15 km), indicating the effective propagation of the perturbation in the tropospheric Hough (1,1) into the MLT region. During 7 of 8 El Niño events (1982, 1986, 1991, 1997, 2002, 2006, and 2009), the Hough (1,1) mode in the tropopause decreased by approximately 15% compared to the climatological mean amplitude, which agrees well with the anomalous Hough (1,1) in the MLT.

As noted earlier, the DW1 tide is primarily excited by the absorption of solar radiation by tropospheric water vapor (Lieberman et al., 2003; Zhang et al., 2010). According to the tidal theory (Volland and Hans, 1988), the heating rate of radiation absorbed by water vapor in the entire troposphere is responsible for the excitation of diurnal migrating tides. Next, we examine the perturbation of the DW1 solar heating source in the SD-WACCM simulation, which potentially contributes to the negative Hough (1,1) tidal anomalies in the tropopause region during El Niño winters. As presented in Figure 5, the anomalous amplitudes of the DW1 heating rate (HR) regressed on the normalized Niño3.4 index are significantly positive (with a maximum of ~0.4 mW/m³ per index) in the upper tropical troposphere (5°S-5°N, 3-12 km) but are significantly negative below 3 km (with a minimum of ~-4 mW/m³ per index). The ENSO-induced changes in the tropospheric DW1 heating forcing may be due to the redistribution of tropospheric convection during El Niño and La Niña winters. During El Niño winters, increased moisture in the upper troposphere due to enhanced tropical precipitation in the central Pacific Ocean (e.g., Hoerling et al., 1997)

删除[cyt]: <sp>

leads to stronger solar heating absorption by water vapor in the middle and upper equatorial troposphere (5–12 km, 10°S–10°N).

On the other hand, heating in the lower troposphere significantly decreased due to less solar radiation below the convective cloud. The DW1 HR regressed on Niño3.4 in the NH (5°N–35°N) is characterized by a very negative coefficient of 3–8 km (with a maximum of ~ -0.3 mW/m³ per index) associated with significantly positive coefficients below 2 km (with a maximum of ~ 3 mW/m³ per index). In the Southern Hemisphere (SH), the distribution of DW1 HR coefficients consists of negative and positive values at different altitudes and latitudes.

Pedatella et al. (2013) adopted the HR in the upper tropical troposphere (5–10 km within $\pm 20^\circ$) to estimate the ENSO-induced variation in the DW1 tidal source. To examine the excitation of the DW1 tide in the lower atmosphere, the HR averaged over several different areas have been selected in previous studies (e.g., altitude range between 900–200 hPa, 1–12 km in Lieberman et al., 2003, and 1000–100 hPa, 0–16 km in Zhang et al., 2010). As suggested in Table 2, the mass-weighted HR averaged over the entire tropical troposphere (0–16 km, 35°N–35°S), which negatively responds to ENSO, is significantly correlated (the correlation coefficient is 0.45) with the DW1 tide in the tropical tropopause region. Although the linear regression coefficient in HR is positive at 5–10 km over the equator (5°N–5°S), the coefficients at 5–30°N(S) are negative (Figure 5), which is opposite of the equator (5°N–5°S). The HR averaged over 5–10 km, 20°N–20°S (the same as in Pedatella et al., 2013) regressed on Niño3.4 is also negative, although it is not significantly correlated with the DW1 tidal variation in the tropopause. The decreased DW1 heating source in the troposphere during El Niño is a primary cause of the suppressed DW1 tide in the tropopause region during winters, which propagates vertically and affects the DW1 tidal variation in the MLT region.

删除[cyt]: <sp>

4.2 Effect of background wind

The zonal wind in the middle atmosphere can modulate tide propagation from the troposphere to the MLT (Forbes and Vincent, 1989). As McLandress (2002b) described, the perturbation of latitudinal shear in the zonal mean zonal wind (zonal mean vorticity) can affect DW1 propagation into the MLT region by causing departures from classical tidal dynamics. The following equation gives the zonal mean vorticity $\bar{\zeta}$ and Coriolis parameter f :

$$\bar{\zeta} = \frac{-1}{a \cos \theta} * \frac{\partial(\bar{u} \cos \theta)}{\partial \theta} \tag{5}$$

$$f = 2\Omega \sin \theta \tag{6}$$

$$R = (\bar{\zeta} + f)/f \tag{7}$$

where a , \bar{u} and θ correspond to the Earth radius, zonal mean zonal wind and latitude, respectively, and Ω is the Earth's rotation rate.

The absolute and planetary vorticity R ratio is equivalent to changing the planet's rotation rate. In classical theory, the vertically propagating DW1 is restricted near the equator due to the planet's rapid rotation. Therefore, a faster rotation rate (positive R anomalies) will suppress the latitudinal band (i.e., waveguide) where DW1 can propagate vertically. On the other hand, the slower rotation rate (negative R anomalies) favors the vertical propagation and is thus able to enhance the amplitude of DW1 at low latitudes (McLandress, 2002b). When the ratio of the absolute and planetary vorticity R -value at a certain height becomes larger, the upward propagation of tide is suppressed, which leads to weaker tides above there.

The MLR coefficient of R on Niño3.4 is illustrated in Figure 6. Below 60 km, the ratio R exhibits negative and positive responses to ENSO depending on different altitudes in the Northern and Southern subtropics. The R response to ENSO is positive at 60-100 km in the Northern subtropics and 65-100 km in the southern subtropics.

删除[cyt]: McCandless

删除[cyt]: Mclandress.

删除[cyt]: ,

删除[cyt]: <sp>

The green thick solid line represents the mean value of the equatorial R (15-30°N and 15-30°S), and it can be seen that the mean R-value response to ENSO is significantly positive at 60-90 km. The increased ratio R in the mesosphere results in the suppressed latitudinal band, which prevents the upward propagation of the DW1 tide during El Niño winters. The correlation coefficient between the R-value and DW1 during the winter of 1979-2014 is ~ -0.33 in the SH and ~ -0.37 in the NH, implying that the R plays a role in modulating the upward propagating of DW1 when no ENSO event occurs. The variation of R and DW1 should not be attributed to the impacts of ENSO separately.

4.3 Effect of gravity wave forcing

In addition to tidal sources and propagation, MLT tidal variability is also affected by interactions with GWs (Liu and Hagan, 1998; Li et al., 2009). GWs are the main driving force of MLT dynamic activity, which influences tidal amplitude and phase (Walterscheid, 1981b; Lu et al., 2012; Liu et al., 2013). The effect of the GW forcing on tides is not fully understood due to the limited observation and lack of high-resolution model simulations that can fully resolve both tides and GWs. In WACCM, the GWs are parameterized, and their tropical sources are interactive and mainly triggered by convection in the tropics (Beres et al., 2005). The GW in the tropics is primarily induced by convection, while the GW in the middle to high latitudes is mainly generated by the frontal systems (Figure S5, S6). Due to this interaction source, the GW drag will likely be modulated by ENSO as the location and size of the ENSO-related convection change. The GW drag far away from the tropospheric source strongly responds to the wind. As mentioned above, we can determine the variation in the resistance of the convection-generated GW in the WACCM. We mainly focus on the latitudinal component of parameterized resistance because it is usually much larger than the meridional component (Yang et al., 2018).

In the NH winter, the DW1 GW drag caused by convection has apparent hemispheric asymmetry: the magnitude is much smaller in the NH than in the SH

删除[cyt]: -
删除[cyt]: (significant at 95% level)
删除[cyt]: is -
删除[cyt]: (significant at 95% level)
删除[cyt]: the correlation coefficient, both of which are significantly correlated. The significantly negative correlation between R and DW1 tide implies
删除[cyt]: modulation of

删除[cyt]: has an important influence on

删除[cyt]: <sp>

(Figure 7a). The zonal wind DW1 tide can be written as $U' = A * \cos(\omega * (t - \varphi) - s\lambda)$, where A and φ are the amplitude and phase of DW1 tide, ω ($\omega = 2\pi/24$) is DW1 frequency, λ is longitude, and s ($s = 2\pi/360$) is the zonal wavenumber of DW1. The time tendency of the zonal wind can be written as $\frac{\partial U'}{\partial t} = \omega * A * \cos(\omega * (t - \varphi) + \frac{\pi}{2} - s\lambda) = \omega * A * \cos(\omega * (t - (\varphi - 6)) - s\lambda)$; (8)

The DW1 tide time tendency phase leads the tide itself by 6 hours. To evaluate the effect of GW forcing on the DW1 tide during DJF, the GW forcing can be calculated as $GW_{\text{forcing}} = GW_{\text{drag}} * \cos(\omega * (\varphi_{GW} - (\varphi_U - 6)))$; (9)

Where GW_{drag} is GW drag, and φ_{GW} and φ_U are the phase of DW1-GW and DW1-U.

The convection-generated GW forcing on the DW1 tide is positive in the southern subtropical upper mesosphere and negative below this tide (60–80 km) during the NH winter (Figure 7b). In the NH mesopause region, the GW forcing on the DW1 tide is positive in the subtropics (15–35°N) and negative in the tropics (0–10° N). This indicates that convection-generated GW forcing will dampen the tides in the tropical MLT and enhance the tides in the NH and SH subtropical regions (Figure 7b). As shown in Figure 8a, the correlation between DW1 U and GW drag from 1979 to 2014 winter (DJF) is only significant in the mesopause region of southern subtropics and the equator. The correlation between DW1 U and GW forcing from 1979 to 2014 winter (DJF) is more significant than 0.7 in the tropical and subtropical MLT (Figure 8b). According to the F-test, the red areas indicate statistical significance above 95%, meaning GW forcing clearly modulates the tide, especially in the Southern subtropics. The linear regression coefficient of Niño3.4 in the GW forcing is significantly negative in the tropical MLT region (Figure 9, 80–100 km), suggesting that the

删除[cyt]: $U' = A * \cos(\omega * (t - \varphi) - s\lambda)$

删除[cyt]: φ

删除[cyt]: ω ($\omega = 2\pi/24$)

删除[cyt]: λ

删除[cyt]: s ($s = 2\pi/360$)

删除[cyt]: wave number

删除[cyt]: $\frac{\partial U'}{\partial t} = \omega * A * \cos(\omega * (t - \varphi) + \frac{\pi}{2} - s\lambda) =$

删除[cyt]: $GW_{\text{forcing}} = GW_{\text{drag}} * \cos(\omega * (\varphi_{GW} - (\varphi_U - 6)))$

删除[cyt]: GW_{drag}

删除[cyt]: φ_{GW}

删除[cyt]: φ_U

删除[cyt]: The

设置格式[cyt]: 图案: 清除(白色)

删除[cyt]: indicates

设置格式[cyt]: 图案: 清除(白色)

删除[cyt]: % level according to F-test,

删除[cyt]: <sp>

decreased GW forcing would lead to a weaker DW1 U amplitude during El Niño winters.

Although parameterized GWs are excited by convection (in the tropics), it is difficult to find a direct cause and effect relationship between ENSO-related tropospheric changes and the GW-induced tidal forcing in the mesosphere. The GW forcing in the MLT not only depends on the generation of waves in the troposphere but also on zonal wind filtering when they propagate upward from the troposphere to the upper mesosphere. However, our study suggests that the ENSO modulation of tidal amplitude can come from the disturbance in tropospheric tidal sources, tidal propagation modulated by zonal wind, and the disturbance of the GW-tidal interaction in the upper mesosphere.

5 Discussion and Summary

The response of the MLT DW1 tide to ENSO is investigated during the Northern winter when ENSO reaches its peak by using satellite observations of temperature profiles and the SD-WACCM simulation. The DW1 temperature amplitude observed by SABER tends to decrease during the NH winter of 4 El Niño events between 2002 and 2020 when El Niño reaches its peak and increases during 3 La Niña events. In SD-WACCM simulations, the DW1 amplitude is suppressed during 7 of 8 El Niño winter (DJF) events from 1979 to 2014.

Possible mechanisms have been proposed to explain the DW1 response to ENSO: (1) the source of tidal excitation in the lower atmosphere and its upward propagation, (2) the impact of background wind variation on the tidal propagation, and (3) interaction between gravity waves and tides. As the Hough (1,1) mode dominates the diurnal migrating tidal temperature in the MLT region, its negative response to ENSO corresponds well with the counterpart at the tropopause. By tracking the downward phase progressive line, the altitude of the excitation source is estimated to be below

删除[cyt]: <sp>

453 15 km. The decreased heating rate in the tropical troposphere (35°S-35°N, 0-16 km)
454 during El Niño contributes to the suppressed DW1 tidal amplitude in the tropical
455 tropopause.

456 As the background variation could modulate the upward propagation of the tide
457 (Forbes and Vincent, 1989; McLandress, 2002a, 2002b), the ratio of the absolute and
458 planetary vorticity R response to ENSO is investigated. The R response to ENSO is
459 significantly positive at 60-90 km, leading to the narrower waveguide and resulting in
460 weaker DW1 amplitude above. However, the regression coefficient of R on the ENSO
461 index is relatively small compared to the mean value of R, which implies that the
462 impact of R on tidal propagation may play a secondary role in the ENSO-DW1
463 connection.

464 In addition to tidal sources and propagation, MLT tidal variability is also
465 dramatically affected by interactions with GWs (Liu and Hagan, 1998; Li et al., 2009).
466 GW forcing considering both the DW1 tidal GWs drag and the phase difference with
467 the DW1 tide is calculated to evaluate the effect of the GW variation on the tide
468 during ENSO winters. The GW forcing response to Niño3.4 is significantly negative
469 in the tropical upper mesosphere, which suggests the GW response to ENSO tends to
470 dampen the MLT DW1 tide during El Niño winter. This tidal-GW interaction could
471 significantly modulate the tidal amplitude, as revealed by early lidar observations (Li
472 et al., 2009; Baumgarten et al., 2018). This could be the most important mechanism of
473 DW1 response in the MLT region to ENSO. However, quantitative evaluation of this
474 interaction is out of the scope of this paper and needs a far more sophisticated model
475 with extremely high resolution to self-generate convective GWs.

476 The weak negative DW1 response to ENSO over the equator may be related to
477 the dissipation or damping of the tide near 95 km. The shorter vertical wavelength
478 would increase the Rayleigh friction coefficient (Forbes et al., 1989), enhancing the
479 tide dissipation. As presented in Table S1, the vertical wavelength of DW1 near 95
480 km is increased (but decreased at around 90 and 100 km), which would suppress the

删除[cyt]: proportional
删除[cyt]: which results in enhancement of
删除[cyt]: <sp>

Rayleigh friction coefficient and lead to less tidal dissipation. Therefore, the less tidal dissipation in this area could result in a relatively weak negative or even positive response to ENSO near 95 km. The interaction of gravity waves and tides may also play a role in modulating the tidal amplitude at different altitudes. However, the SD-WACCM simulation failed to perform a similar tidal response near 95 km as SABER observations. Further investigation is needed with more detailed GW observations or the improved GW parameterization scheme and higher vertical resolution in the model simulation.

设置格式[cyt]: 字体: 加粗, 字距调整: 四号

Data availability

删除[cyt]:

SABER datasets are available at <http://saber.gats-inc.com/data.php>, and ECMWF datasets used here are obtained at <http://apps.ecmwf.int/datasets/data>.

Author contributions

YC and CY designed the study, performed data analysis, prepared the figures, and wrote the manuscript. TL initiated the research and contributed to supervision and interpretation. JY and JR contributed to editing the manuscript. XD contributed to the interpretation. All authors contributed to the discussion and interpretation.

Competing interests

The authors declare that they have no conflict of interest.

Acknowledgments

This work was supported by the National Natural Science Foundation of China grants (42130203, 41874180, 41974175), the B-type Strategic Priority Program of the Chinese Academy of Sciences, Grant No. XDB41000000, and the pre-research

删除[cyt]: funded

删除[cyt]: , 41874180), and

删除[cyt]: <sp>

506 project on Civil Aerospace Technologies No. D020105 funded by China's National
507 Space Administration. JY and JMR's work is supported by the National Science
508 Foundation grant AGS-1901126.

删除[cyt]: <sp>

Reference

- Auclair-Desrotour, P. , Laskar, J. , & Mathis, S.: Atmospheric tides and their consequences on the rotational dynamics of terrestrial planets. *EAS Publications Series*, 82 (2019) 81-90; <https://doi.org/10.1051/eas/1982008>, 2017.
- Baumgarten, K., Gerding, M., Baumgarten G., & Luebken, F.-J.: Temporal variability of tidal and gravity waves during a record long 10-day continuous lidar sounding. *Atmospheric chemistry and physics*, 18, 371–384; <https://doi.org/10.5194/acp-18-371-2018>, 2018
- Beres, J. H., Garcia, R. R., Boville, B. A., & Sassi, F: Implementation of a gravity wave source spectrum parameterization dependent on the properties of convection in the Whole Atmosphere Community Climate Model (WACCM). *Journal of Geophysical Research*, 110, D10108; <https://doi.org/10.1029/2004JD005504>, 2015.
- Calvo-Fernández, N., Herrera, R. G., Puyol, D. G. , Martín, E. H., García, R. R., Presa, L. G. & Rodríguez, P. R: Analysis of the enso signal in tropospheric and stratospheric temperatures observed by msu, 1979-2000. *Journal of Climate*, 17(20), 3934-3946; [http://doi.org/10.1175/1520-0442\(2004\)017<3934:aotesi>2.0.co;2](http://doi.org/10.1175/1520-0442(2004)017<3934:aotesi>2.0.co;2), 2004.
- Chapman, S., & Lindzen, R. S.: Atmospheric Tides, 201 pp., D. Reidel, Norwell, Mass., 1970.
- Davis, R. N., Du, J., Smith, A. K., Ward, W. E., & Mitchell, N. J.: The diurnal and semidiurnal tides over Ascension Island (8°S, 14°W) and their interaction with the stratospheric QBO: Studies with meteor radar, eCMAM and WACCM. *Atmospheric Chemistry and Physics*, 13(18), 9543–9564; <https://doi.org/10.5194/acp-13-9543-2013>, 2013.
- Dhadly, M. S., Emmert, J. T., Drob, D. P., McCormack, J. P., & Niciejewski, R.: Short-term and interannual variations of migrating diurnal and semidiurnal tides in the mesosphere and lower thermosphere. *Journal of Geophysical Research: Space Physics*, 123, 7106–7123; <https://doi.org/10.1029/2018JA025748>, 2018.

删除[cyt]: <sp>

Forbes, J. M.: Tidal and planetary waves. *Geophysical Monograph Series*, 87;
<https://doi.org/10.1029/GM087p0067>, 1995.

Forbes, J. M. , & Vincent, R. A.: Effects of mean winds and dissipation on the diurnal
propagating tide: an analytic approach. *Planetary & Space Science*, 37(2),
197-209; [https://doi.org/10.1016/0032-0633\(89\)90007-X](https://doi.org/10.1016/0032-0633(89)90007-X), 1989.

Gan, Q., Du, J., Ward, W. E., Beagley., S. R., Fomichev., V. I., & Zhang, S.:
Climatology of the diurnal tides from eCMAM30 (1979 to 2010) and its
comparisons with SABER. *Earth Planets Space* 66:103;
<https://doi.org/10.1186/1880-5981-66-103>, 2014.

Garcia, R. R., Marsh, D. R., Kinnison, D. E., Boville, B. A., & Sassi, F.: Simulation of
secular trends in the middle atmosphere, 1950–2003.
Journal of Geophysical Research, 112, D09301;
<https://doi.org/10.1029/2006JD007485>, 2007.

Gray, W. M.: Atlantic seasonal hurricane frequency: Part I: El Niño and 30 mb
quasi-biennial oscillation influences. *Mon. Wea. Rev.*, 112, 1649–1668;
[https://doi.org/10.1175/1520-0493\(1984\)112<1649:ASHFPI>2.0.CO;2](https://doi.org/10.1175/1520-0493(1984)112<1649:ASHFPI>2.0.CO;2), 1984.

Gurubaran, S., & Rajaram, R.: Long-term variability in the mesospheric tidal winds
observed by MF radar over Tirunelveli (8.7°N, 77.8°E). *Geophysical Research
Letters*, 26(8), 1113–1116; <https://doi.org/10.1029/1999GL900171>, 1999.

Gurubaran, S., Rajaram, R., Nakamura, T., & Tsuda, T.: Interannual variability of
diurnal tide in the tropical mesopause region: a signature of the El Niño-Southern
Oscillation (ENSO). *Geophysical Research Letters* 32(13);
<https://doi.org/10.1029/2005gl022928>, 2005.

Hagan, M.E., Burrage, M.D., Forbes, J.M. et al.: QBO effects on the diurnal tide in
the upper atmosphere. *Earth Planet Space*, 51, 571–578;
<http://doi.org/10.1186/BF03353216>, 1999.

Hagan, M. E., and J. M. Forbes.: Migrating and nonmigrating diurnal tides in the
middle and upper atmosphere excited by tropospheric latent heat release, *J.
Geophys. Res.*, 107(D24), 4754; <https://doi.org/10.1029/2001JD001236>, 2002.

删除[cyt]: <sp>

Hoerling, M. P., A. Kumar, and M. Zhong.: El Niño, La Niña, and the nonlinearity of their teleconnections, *Journal of Climate*, 10, 1769–1786; [https://doi.org/10.1175/1520-0442\(1997\)010<1769:ENOLNA>2.0.CO;2](https://doi.org/10.1175/1520-0442(1997)010<1769:ENOLNA>2.0.CO;2), 1997.

Kissell, R. & Poserina, J.: Optimal Sports Math, Statistics, and Fantasy; <https://doi.org/10.1016/B978-0-12-805163-4.00002-5>, 2017.

Kogure, M., & Liu, H.: DW1 tidal enhancements in the equatorial MLT during 2015 El Niño: The relative role of tidal heating and propagation. *Journal of Geophysical Research: Space Physics*, 126, e2021JA029342; <https://doi.org/10.1029/2021JA029342>, 2021.

Kunz, A., Pan, L., Konopka, P., Kinnison, D., & Tilmes, S.: Chemical and dynamical discontinuity at the extratropical tropopause based on START08 and WACCM analyses. *Journal of Geophysical Research*, 116, D24302; <https://doi.org/10.1029/2011JD016686>, 2011.

Lieberman, R. S., Ortland, D. A., & Yarosh, E. S.: Climatology and interannual variability of diurnal water vapor heating. *Journal of Geophysical Research: Atmospheres* 108(D3); <https://doi.org/10.1029/2002jd002308>, 2003.

Lieberman, R. S., Riggin, D. M., Ortland, D. A., Nesbitt, S. W., & Vincent, R. A.: Variability of mesospheric diurnal tides and tropospheric diurnal heating during 1997–1998. *Journal of Geophysical Research: Atmospheres* 112(D20); <https://doi.org/10.1029/2007jd008578>, 2007.

Li, T., She, C. -Y., Liu, H., Yue, J., Nakamura, T., Krueger, D. A.: Observation of local tidal variability and instability, along with dissipation of diurnal tidal harmonics in the mesopause region over Fort Collins, Colorado (41°N, 105°W). *Journal of Geophysical Research: Atmospheres* (1984–2012), 114(D6); <https://doi.org/10.1029/2008jd011089>, 2009.

Li, T., Calvo, N., Yue, J., Dou, X., Russell III, J. M., Mlynczak, M. G., She, C.-Y., & Xue, X. (2013). Influence of El Niño-Southern Oscillation in the mesosphere. *Geophysical Research Letters*, 40, 3292–3296, <https://doi.org/10.1002/grl.50598>.

596 Li, T., Calvo, N., Yue, J., Russell, J. M. I., Smith, A. K., Mlynczak, M. G., Chandran,
 597 A., Dou, X., & Liu, A. Z.: Southern Hemisphere summer mesopause responses
 598 to El Niño-Southern Oscillation. *Journal of Climate*, 29(17),
 599 6319– 6328; <https://DOI.org/10.1175/JCLI-D-15-0816.1>, 2016.

600 Liu, A. Z., Lu, X., & Franke, S. J.: Diurnal variation of gravity wave momentum
 601 flux and its forcing on the diurnal tide. *Journal of Geophysical Research –*
 602 *Atmospheres*, 118, 1668–1678; <https://doi.org/10.1029/2012JD018653>, 2013.

603 Liu, H., Sun, Y.-Y., Miyoshi, Y., & Jin, H.: ENSO effects on MLT diurnal tides: A
 604 21 year reanalysis data-driven GAIA model simulation. *Journal of Geophysical*
 605 *Research: Space Physics*, 122, 5539–5549;
 606 <https://doi.org/10.1002/2017JA024011>, 2017.

607 Liu, H.-L., Wang, W., Richmond, A. D., & Roble, R. G.: Ionospheric variability due
 608 to planetary waves and tides for solar minimum conditions. *Journal of*
 609 *Geophysical Research: Space Physics*, 115, A00G01;
 610 <https://doi.org/10.1029/2009JA015188>, 2010.

611 Liu, H.-L., & Hagan, M. E.: Local heating/cooling of the mesosphere due to gravity
 612 wave and tidal coupling. *Geophysical Research Letters*, 25, 2941–2944;
 613 <https://doi.org/10.1029/98GL02153>, 1998.

614 Lu, X., Liu, A. Z., Swenson, G. R., Li, T., Leblanc, T., & McDermid, I. S.: Gravity
 615 wave propagation and dissipation from the stratosphere to the lower
 616 thermosphere. *Journal of Geophysical Research: Atmospheres*, 114, D11101;
 617 <https://doi.org/10.1029/2008JD010112>, 2009.

618 Lu, X., Liu, H.-L., Liu, A. Z., Yue, J., McInerney, J. M., & Li, Z.: Momentum budget
 619 of the migrating diurnal tide in the Whole Atmosphere Community Climate
 620 Model at vernal equinox. *Journal of Geophysical Research*, 117, D07112;
 621 <https://doi.org/10.1029/2011JD017089>, 2012.

622 Lu, X., Liu, A. Z., Oberheide, J., Wu, Q., Li, T., Li, Z., et al.: Seasonal variability of
 623 the diurnal tide in the mesosphere and lower thermosphere over Maui, Hawaii

删除[cyt]: <sp>

(20.7°N, 156.3°W). *Journal of Geophysical Research*, 116, D17103;
<https://doi.org/10.1029/2011JD015599>, 2011.

Mayr H.G., Mengel J.G.: Interannual variations of the diurnal tide in the mesosphere
 generated by the quasi-biennial oscillation, *J Geophys Res* 110:D10111;
<http://doi.org/10.1029/2004JD005055>, 2005.

McLandress, C., Shepherd, G. G., & Solheim, B. H.: Satellite observations of
 thermospheric tides: Results from the wind imaging interferometer on UARS.
Journal of Geophysical Research: Atmospheres 101(D2):4093–4114;
<https://doi.org/10.1029/95jd03359>, 1996.

McLandress, C.: Interannual variations of the diurnal tide in the mesosphere induced
 by a zonal- mean wind oscillation in the tropics, *Geophys. Res. Lett.*, 29(9);
<http://doi.org/10.1029/2001GL014551>, 2002a.

McLandress, C.: The seasonal variation of the propagating diurnal tide in the
 mesosphere and lower thermosphere. Part II: The role of tidal heating and zonal
 mean winds, *J. Atmos. Sci.*, 59(5), 907–922;
[https://doi.org/10.1175/1520-0469\(2002\)059<0907:Tsvotp>2.0.Co;2](https://doi.org/10.1175/1520-0469(2002)059<0907:Tsvotp>2.0.Co;2), 2002b.

Mertens, C. J., Mlynczak, M. G., Lopez-Puertas, M., Wintersteiner, P. P., Picard, R.
 H., Winick, J. R., & Gordley, L. L.: Retrieval of mesospheric and lower thermos
 pheric kinetic temperature from measurements of CO₂ 15 μm Earth limb
 emission under non-LTE conditions, *Geophysical Research Letters*, 28(7),
 1391-1394; <https://doi.org/10.1029/2000GL012189>, 2001.

Mertens, C. J., Schmidlin, F. J., Goldberg, R. A., Remsberg, E. E., Pesnell, W. D.,
 Russell, J. M., Mlynczak, M. G., Lopez-Puertas, M., Wintersteiner, P. P., Picard,
 R. H., Winick, J. R., & Gordley, L. L.: SABER observations of mesospheric
 temperatures and comparisons with falling sphere measurements taken during
 the 2002 summer MaCWAVE campaign. *Geophysical Research Letters* 31(3);
<https://doi.org/10.1029/2003gl018605>, 2004.

Pedatella, N. M., & Liu, H. L.: Tidal variability in the mesosphere and lower
 thermosphere due to the El Niño-Southern Oscillation. *Geophysical Research*
Letters 39; <https://doi.org/10.1029/2012gl053383>, 2012.

删除[cyt]: <sp>

654 Pedatella, N. M., & Liu, H. L.: Influence of the El Niño Southern Oscillation on the
655 middle and upper atmosphere. *Journal of Geophysical Research: Atmospheres*
656 118(5):2744–2755; <https://doi.org/10.1002/Jgra.50286>, 2013.

657 Ramesh, K., Smith, A. K., Garcia, R. R., Marsh, D. R., Sridharan, S., & Kishore
658 Kumar, K.: Long-term variability and tendencies in migrating diurnal tide from
659 WACCM6 simulations during 1850–2014. *Journal of Geophysical Research:*
660 *Atmospheres*, 125, e2020JD033644; <https://doi.org/10.1029/2020JD033644>,
661 2020.

662 Randel, W. J. , Shine, K. P. , Austin, J. , Barnett, J. , Claud, C. , & Gillett, N. P.: An
663 update of observed stratospheric temperature trends. *Journal of Geophysical*
664 *Research: Atmospheres*. 114, D02107; <https://doi.org/10.1029/2008JD010421>,
665 2009.

666 Rezac, L., Jian, Y., Yue, J., Russell III, M. J., Kutepov, A., Garcia, R., Walker, K.,
667 and Bernath, P.: Validation of the global distribution of CO₂ volume mixing
668 ratio in the mesosphere and lower thermosphere from SABER, *J. Geophys. Res.*
669 *Atmos.*, 120, 12,067– 12,081;
670 <https://doi.org/10.1002/2015JD023955>, 2015.

671 Sassi, F., Kinnison, D., Boville, B., Garcia, R., Roble, R.: Effect of el niño–southern
672 oscillation on the dynamical, thermal, and chemical structure of the middle
673 atmosphere. *Journal of Geophysical Research*, 109(D17), D17108;
674 <http://doi.org/10.1029/2003jd004434>, 2004.

675 Smith, A. K.: Global Dynamics of the MLT. *Surveys in Geophysics*, 33(6):
676 1177–1230; <https://doi.org/10.1007/s10712-012-9196-9>, 2012.

677 Smith, A. K., Pedatella, N. M., Marsh, D. R., & Matsuo, T.: On the Dynamical
678 Control of the Mesosphere–Lower Thermosphere by the Lower and Middle
679 Atmosphere, *Journal of the Atmospheric Sciences*, 74(3), 933–947;
680 <https://doi.org/10.1175/JAS-D-16-0226.1>, 2017.

681 Sridharan, S., Tsuda, T., & Gurubaran, S.: Long-term tendencies in the
682 mesosphere/lower thermosphere mean winds and tides as observed by
683 medium-frequency radar at Tirunelveli (8.7° N, 77.8° E). *Journal of Geophysical*

删除[cyt]: <sp>

684 *Research: Atmospheres*, 115(D8);
685 <http://doi.org/10.1029/2008JD011609>, 2010.

686 Sridharan, S.: Seasonal variations of low-latitude migrating and nonmigrating diurnal
687 and semidiurnal tides in TIMED-SABER temperature and their relationship with
688 source variations. *Journal of Geophysical Research: Space Physics*, 124,
689 3558–3572;
690 <https://doi.org/10.1029/2018JA026190>, 2019.

691 Sridharan, S.: Equatorial upper mesospheric mean winds and tidal response to strong
692 El Niño and La Niña. *Journal of Atmospheric and Solar-Terrestrial Physics*, 202,
693 105270;
694 <https://doi.org/10.1016/j.jastp.2020.105270>, 2020.

695 Vincent, R. A., Kovalam, S., Fritts, D. C., & Isler, J. R.: Long-term MF radar
696 observations of solar tides in the low-latitude mesosphere: Interannual variability
697 and comparisons with GSWM. *Journal of Geophysical Research*, 103(D8),
698 8667–8683; <https://doi.org/10.1029/98JD00482>, 1998.

699 Vitharana, A., Du, J., Zhu, X., Oberheide, J., & Ward, W. E.: Numerical prediction of
700 the migrating diurnal tide total variability in the mesosphere and lower
701 thermosphere. *Journal of Geophysical Research: Space Physics*, 126,
702 e2021JA029588; <https://doi.org/10.1029/2021JA029588>, 2021.

703 Volland & Hans. *Atmospheric Tidal and Planetary Waves*[M]. *Springer Netherlands*,
704 1988.

705 Wallace, J. M., Panetta, R. L., & Estberg J.: Representation of the equatorial
706 quasi-biennial oscillation in EOF phase space. *Journal of the Atmospheric*
707 *Sciences*, 50, 1751 – 1762;
708 [https://doi.org/10.1175/1520-0469\(1993\)050<1751:ROTESQ>2.0.CO;2](https://doi.org/10.1175/1520-0469(1993)050<1751:ROTESQ>2.0.CO;2), 1993.

709 Walterscheid, R. L.: Inertia-gravity wave induced accelerations of mean flow having
710 an imposed periodic component: Implications for tidal observations in the meteor
711 region. *Journal of Geophysical Research: Atmospheres*, 86, 9698 – 9706;
712 <https://doi.org/10.1029/JC086iC10p09698>, 1981a.

删除[cyt]: <sp>

Walterscheid, R. L.: Dynamical cooling induced by dissipating internal gravity waves. *Geophysical Research Letters*, 8(12), 1235 – 1238; <https://doi.org/10.1029/GL008i012-p01235>, 1981b.

Xu, J. Y., Liu, H. L., Yuan, W., Smith, A. K., Roble, R. G., Mertens, C. J., Russell, J. M., & Mlynczak, M. G.: Mesopause structure from thermosphere, ionosphere, mesosphere, energetics, and dynamics (TIMED)/sounding of the atmosphere using broadband emission radiometry (SABER) observations. *Journal of Geophysical Research: Atmospheres* 112 (D9); <https://doi.org/10.1029/2006jd007711>, 2007a.

Xu, J. Y., Smith, A. K., Yuan, W., Liu, H. L., Wu, Q., Mlynczak, M. G., Russell, J. M.: Global structure and long-term variations of zonal mean temperature observed by TIMED/SABER. *Journal of Geophysical Research: Atmospheres*, 112, D24106; <https://doi.org/10.1029/2007jd008546>, 2007b.

Xu, J., Smith, A. K., Liu, H.-L., Yuan, W., Wu, Q., Jiang, G., Mlynczak, G. M., Russell III, J. M., and Franke, S. J.: Seasonal and quasi-biennial variations in the migrating diurnal tide observed by Thermosphere, Ionosphere, Mesosphere, Energetics and Dynamics (TIMED), *J. Geophys. Res.*, 114, D13107; doi:10.1029/2008JD011298, 2009.

Yang, C., Smith, A. K., Li, T., & Dou, X.: The effect of the Madden-Julian oscillation on the mesospheric migrating diurnal tide: A study using SD-WACCM. *Geophysical Research Letters*, 45, 5105–5114; <https://doi.org/10.1029/2018GL077956>, 2018.

Yulaeva, E., & Wallace, J. M.: The signature of ENSO in global temperature and precipitation fields derived from the microwave sounding unit. *Journal of climate*, 7(11), 1719-1736; [https://doi.org/10.1175/1520-0442\(1994\)007<1719:TSOEIG>2.0.CO;2](https://doi.org/10.1175/1520-0442(1994)007<1719:TSOEIG>2.0.CO;2), 1994.

Zhang, X., Forbes, J. M., & Hagan, M. E.: Longitudinal variation of tides in the MLT region: 1. Tides driven by tropospheric net radiative heating. *Journal of Geophysical Research: Space Physics*, 115, A06316; <https://doi.org/10.1029/2009JA014897>, 2010.

删除[cyt]: <sp>

743 Zhou, X., Wan, W., Yu, Y., Ning, B., Hu, L., and Yue, X.: New approach to estimate
744 tidal climatology from ground-and space-based observations. *Journal of*
745 *Geophysical Research: Space Physics*, 123, 5087– 5101;
746 <http://doi.org/10.1029/2017JA024967>, 2018.

747

748

删除[cyt]: <sp>

749 **Table 1.** The list of ENSO years with corresponding Niño3.4 indices and anomaly DW1
750 temperature amplitudes of the SD-WACCM simulations averaged over 10°S-10°N at 100 km.

El Niño events	Niño3.4 index	SD-WACCM anomalous DW1 T AMP (K)
1982-1983	2.14	-0.22
1986-1987	1.11	-2.90
1991-1992	1.69	-1.56
1994-1995	1.22	1.56
1997-1998	2.33	-1.87
2002-2003	1.37	-0.55
2006-2007	1.09	-1.30
2009-2010	1.43	-1.82
AVG	1.54	-0.96

751

752

753 **Table 2.** The correlation coefficient between the DW1 T amplitude at 15 km and the
754 mass-weighted HR in different areas during the winters of 1979-2014. The bold numbers indicate
755 that the correlation coefficients are significant at 95%. The MLR coefficient on the normalized
756 Niño3.4 index (10^{-3} mw m⁻³ index⁻¹) is also exhibited.

Altitude and latitude ranges	0-16 km, 35°N-35°S	0-12 km, 35°N-35°S	5-10 km, 35°N-35°S	5-10 km, 20°N-20°S
Correlation coefficient	0.45	0.36	0.32	0.32
MLR coefficient on Niño3.4	-3	-10	-26	-9

757

Figure captions

Figure 1. (a) The average DW1 temperature amplitude of SABER observation during the 2002-2013 winter (DJF, Dec-Jan-Feb). (b) the same as (a), but for SD-WACCM.

Figure 2. (a) The residual DW1 temperature amplitude of SABER observations averaged over 10°S-10°N at 100 km ~~from 2002 to 2021~~. (b) Same as in (a) but for SD-WACCM. (c) Niño3.4 index. Dashed lines represent ENSO events. The red solid and hollow blue arrows denote the El Niño and La Niña events.

Figure 3. The linear regression coefficient of normalized Niño3.4 in SABER (a) and SD-WACCM (b) winter DW1-T. The contour interval is 0.2 K for SABER and 0.1 K for SD-WACCM. Solid lines and red shadings denote the positive responses, while dashed lines and blue shadings denote the negative responses; the grey regions indicate where the response is insignificant at the 95% level according to the F test.

Figure 4. (a) The solid red line indicates the anomalous DW1 temperature amplitude of SD-WACCM simulations averaged over 10°S-10°N at 100 km during the 1979-2013 winter (DJF). The blue dotted line indicates the Hough (1,1) mode of the DW1 temperature amplitude residual at 100 km during the 1979-2013 winter (DJF). (b) The thin black dotted line indicates the Hough (1,1) DW1-T phase of SD-WACCM simulations at 0-100 km during the 1979-2013 winter (DJF). The thick black horizontal line indicates the standard deviation of the DW1-T phase. The solid red line is the same but for El Niño winter. (c) The solid blue line is the same as in (a), and the black dotted line is the same but for 15 km.

Figure 5. The linear regression coefficient of normalized Niño3.4 in SD-WACCM heating amplitude (mW/m³ per index) during 1979-2013 winters (DJF). Solid lines and red shadings denote the positive responses, while dashed lines and blue shadings denote the negative responses; the grey regions indicate where the response is insignificant at the 95% level according to the F test.

Figure 6. The linear regression coefficient of normalized Niño3.4 in δR (the anomaly of the ratio of the absolute to planetary vorticity). The thin dashed red, blue, and green lines denote the averages of the Northern Hemisphere (from 15°N to 30°N), Southern Hemisphere (from 15°S to 30°S), and the whole (15-30°N and 15-30°S), respectively. The thick, solid lines denote

删除[cyt]: during

删除[cyt]: -

设置格式[cyt]: 字体: 五号

设置格式[cyt]: 字体: 五号

删除[cyt]: <sp>

787 confidence levels higher than 95% for the F test.

788 **Figure 7.** (a) Gravity Wave (GW) drag due to convection on the amplitude of DW1 tidal U during
789 the winter (DJF). (b) The same as (a), but for GW forcing.

790 **Figure 8.** Correlation (a) between DW1 U and GW drag, (b) between DW1 U and GW forcing
791 from 1979 to 2014 winter (DJF). Solid lines and red shadings denote the positive responses, while
792 dashed lines and blue shadings denote the negative responses; the grey regions indicate where the
793 response is insignificant at the 95% level according to the F test.

794 **Figure 9.** The linear regression coefficient of normalized Niño3.4 in the GW forcing on the
795 amplitude of DW1-U during the 1979-2013 winters (DJF). Solid lines and red shadings denote the
796 positive responses, while dashed lines and blue shadings denote the negative responses; the grey
797 regions indicate where the response is insignificant at the 95% level according to the F test.

798

799

Figures

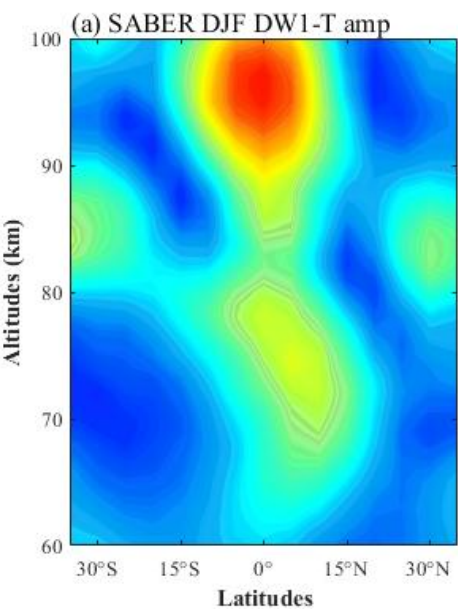
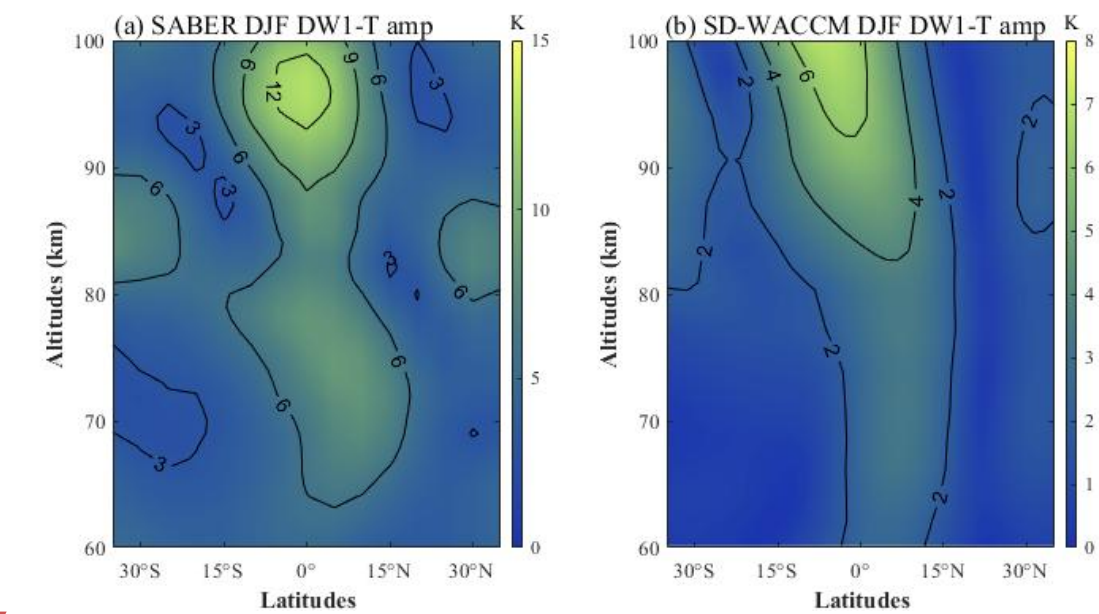
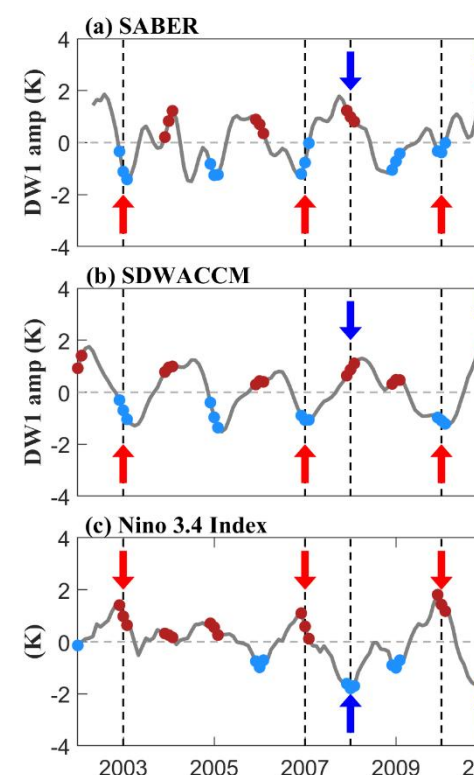
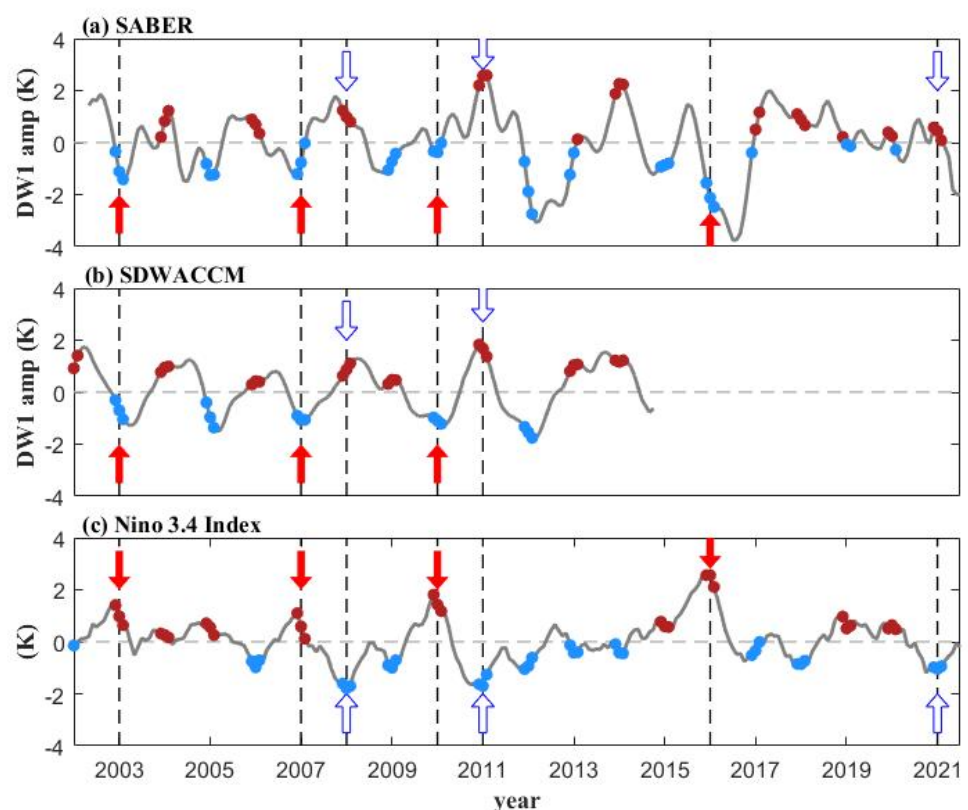


Figure 1. (a) The average DW1 temperature amplitude of SABER observation during the 2002-2013 winter (DJF, Dec-Jan-Feb). (b) the same as (a), but for SD-WACCM.

删除[cyt]: <sp>



删除[cyt]:

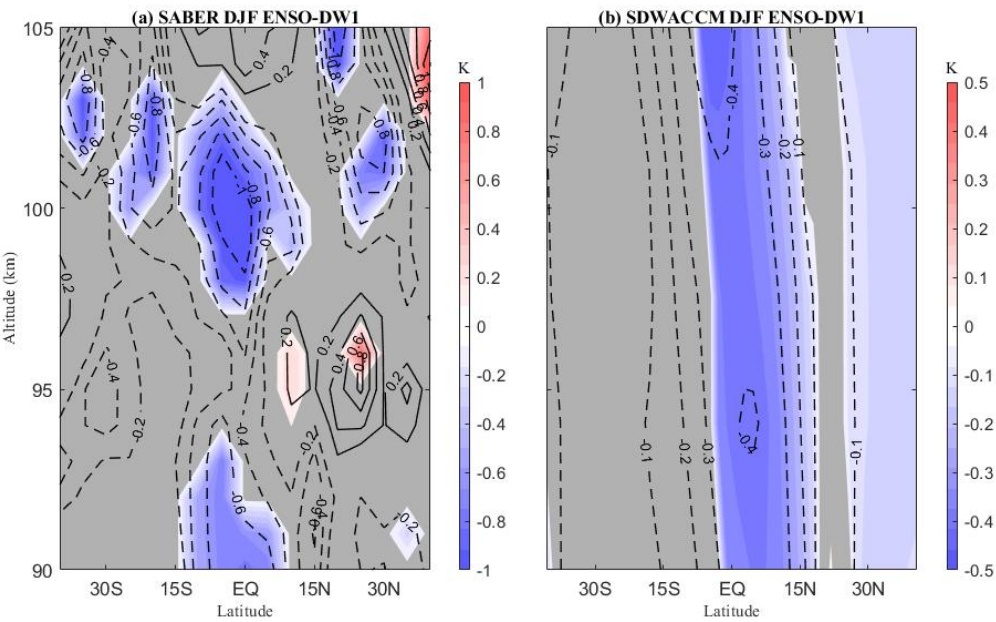
删除[cyt]: during

删除[cyt]: -

设置格式[cyt]: 字体: 五号

设置格式[cyt]: 字体: 五号

删除[cyt]: <sp>



812
813 **Figure 3.** The linear regression coefficient of normalized Niño3.4 in SABER (a) and SD-WACCM
814 (b) winter DW1-T. The contour interval is 0.2 K for SABER and 0.1 K for SD-WACCM. Solid
815 lines and red shadings denote the positive responses, while dashed lines and blue shadings denote
816 the negative responses; the grey regions indicate where the response is insignificant at the 95%
817 level according to the F test.

818

819

820

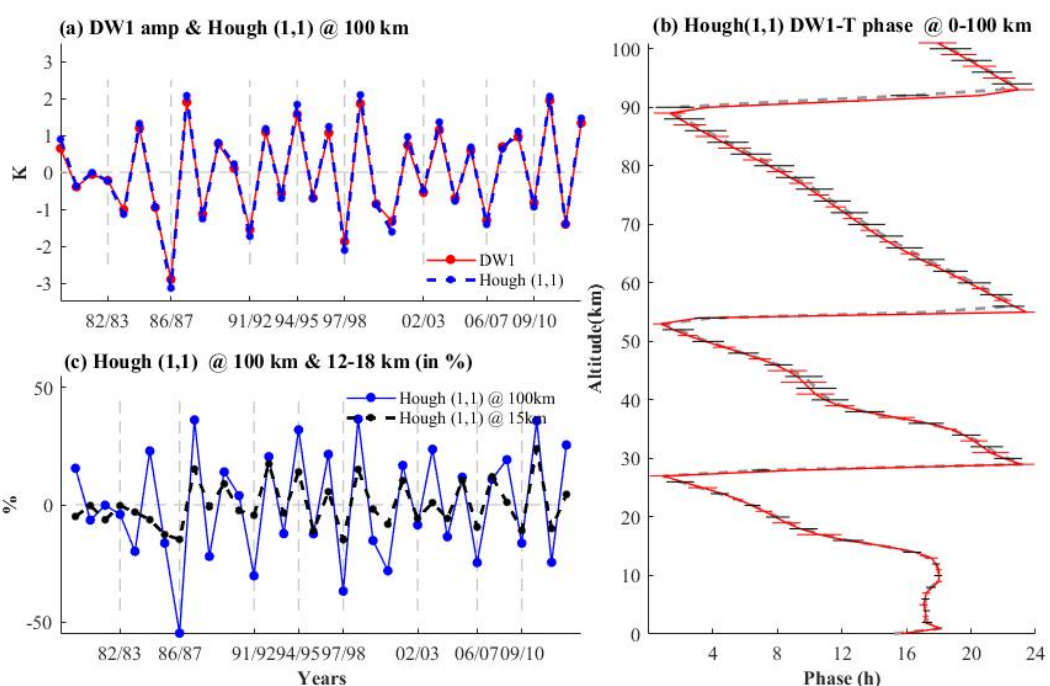
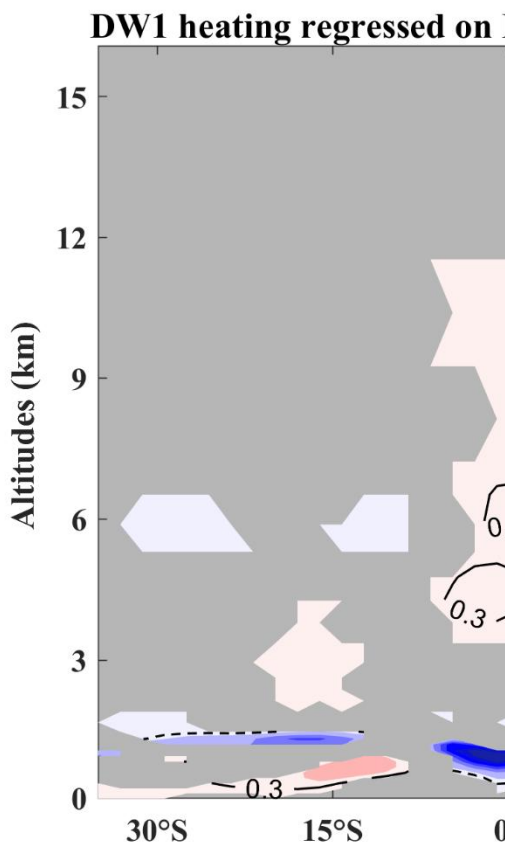


Figure 4. (a) The solid red line indicates the anomalous DW1 temperature amplitude of SD-WACCM simulations averaged over 10°S-10°N at 100 km during the 1979-2013 winter (DJF). The blue dotted line indicates the Hough (1,1) mode of the DW1 temperature amplitude residual at 100 km during the 1979-2013 winter (DJF). (b) The thin black dotted line indicates the Hough (1,1) DW1-T phase of SD-WACCM simulations at 0-100 km during the 1979-2013 winter (DJF). The thick black horizontal line indicates the standard deviation of the DW1-T phase. The solid red line is the same but for El Niño winter. (c) The solid blue line is the same as in (a), and the black dotted line is the same but for 15 km.



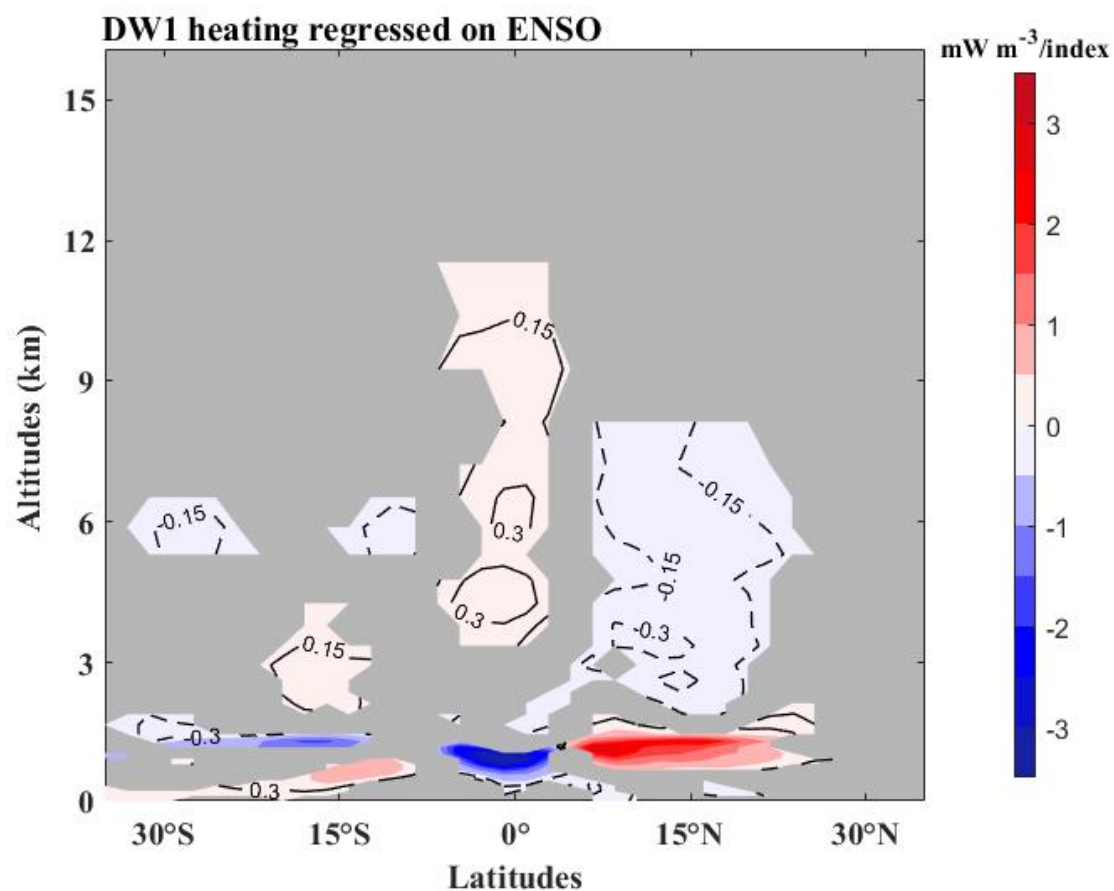
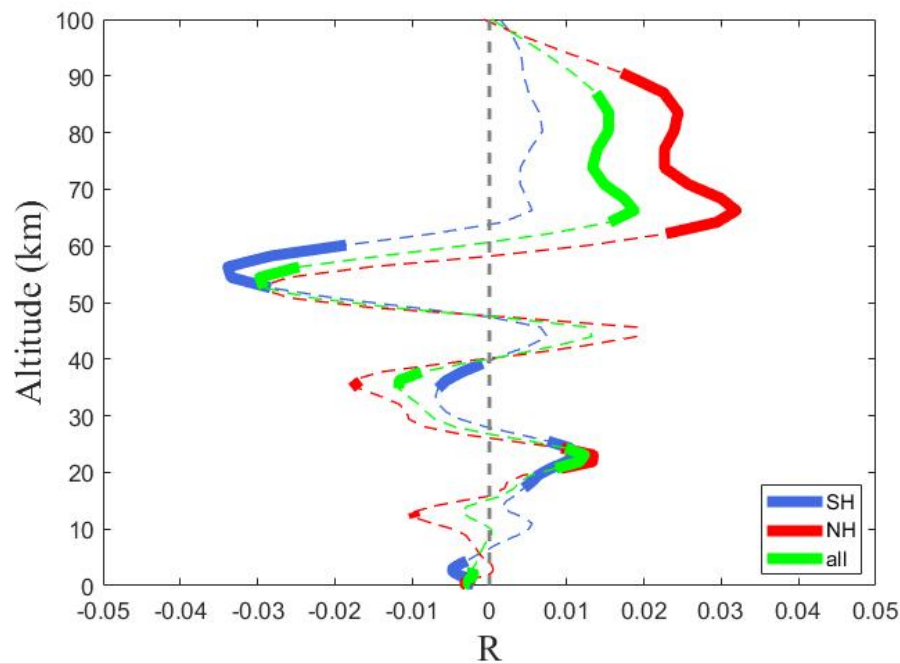
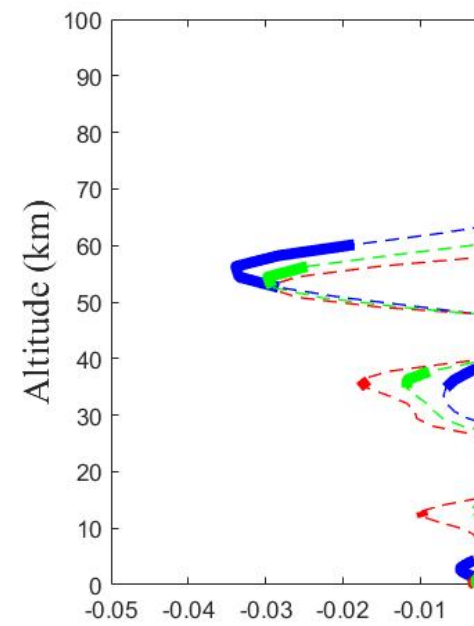


Figure 5. The linear regression coefficient of normalized Niño3.4 in SD-WACCM heating amplitude (mW/m^3 per index) during 1979-2013 winters (DJF). Solid lines and red shadings denote the positive responses, while dashed lines and blue shadings denote the negative responses; the grey regions indicate where the response is insignificant at the 95% level according to the F test.

删除[cyt]: <sp>



删除[cyt]:



删除[cyt]: <sp>

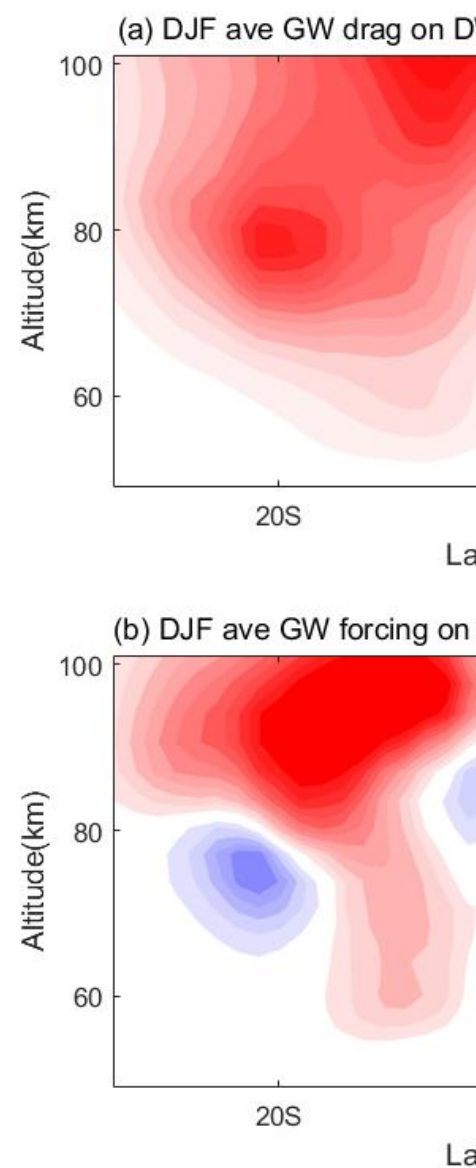
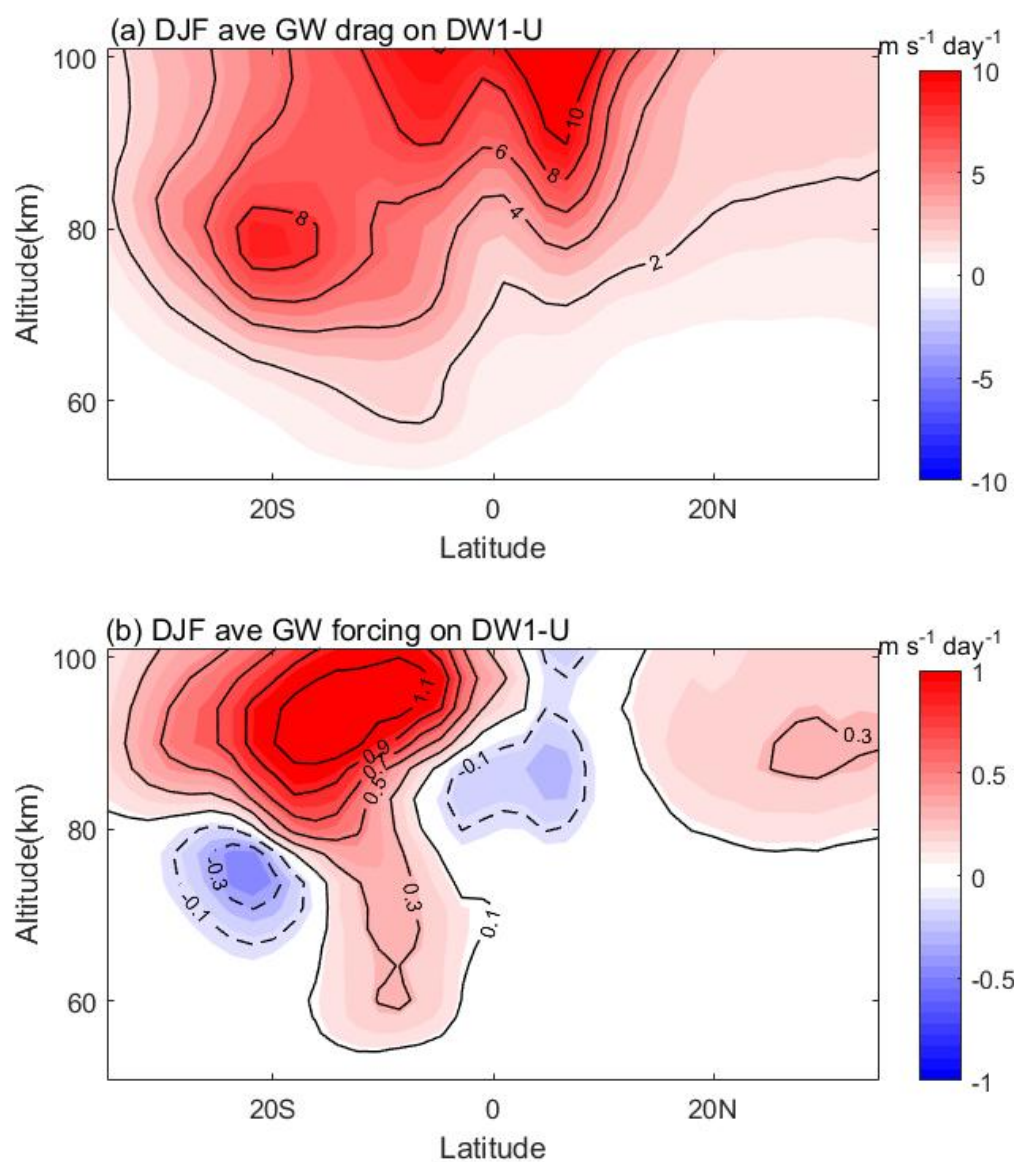


Figure 7. (a) Gravity Wave (GW) drag due to convection on the amplitude of DW1 tidal U during the winter (DJF). (b) The same as (a), but for GW forcing.

删除[cyt]:

删除[cyt]: <sp>

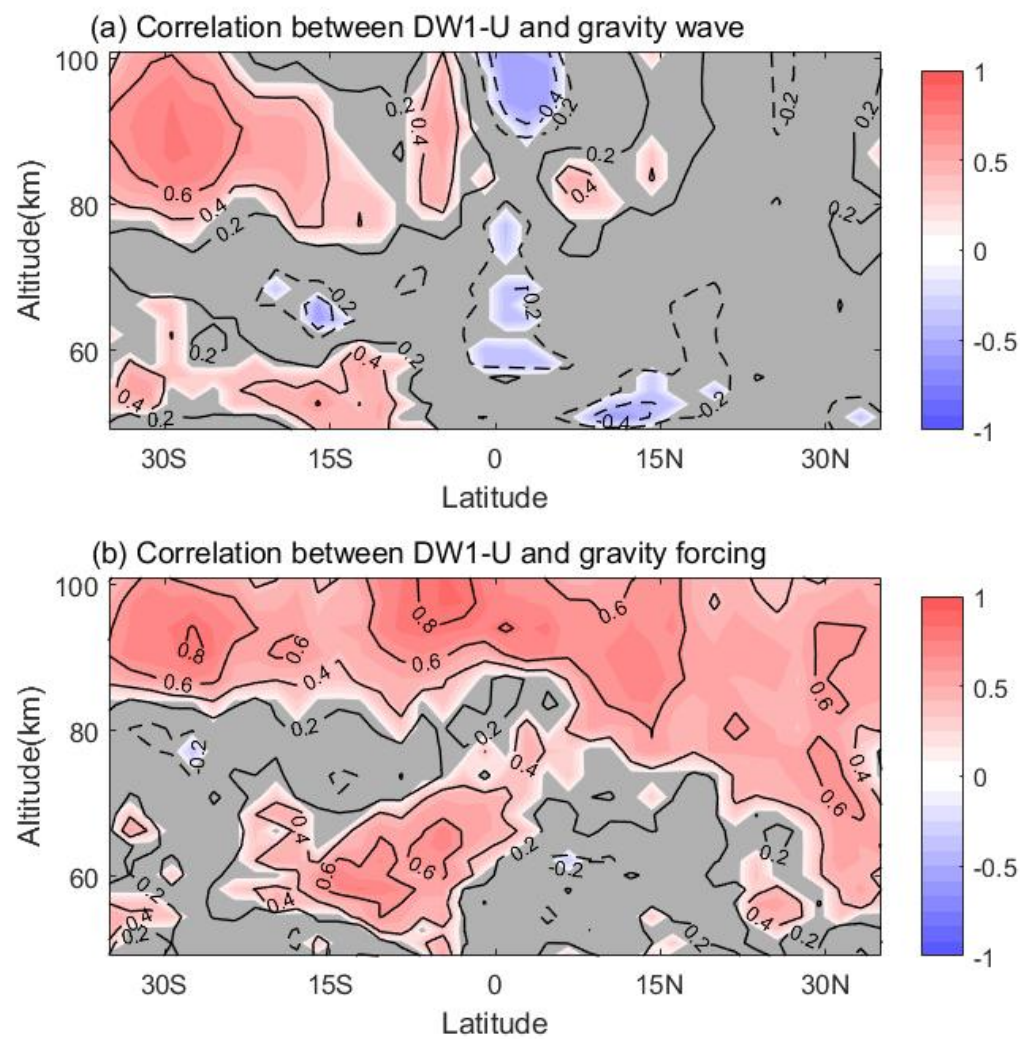


Figure 8. Correlation (a) between DW1 U and GW drag, (b) between DW1 U and GW forcing from 1979 to 2014 winter (DJF). Solid lines and red shadings denote the positive responses, while dashed lines and blue shadings denote the negative responses; the grey regions indicate where the response is insignificant at the 95% level according to the F test.

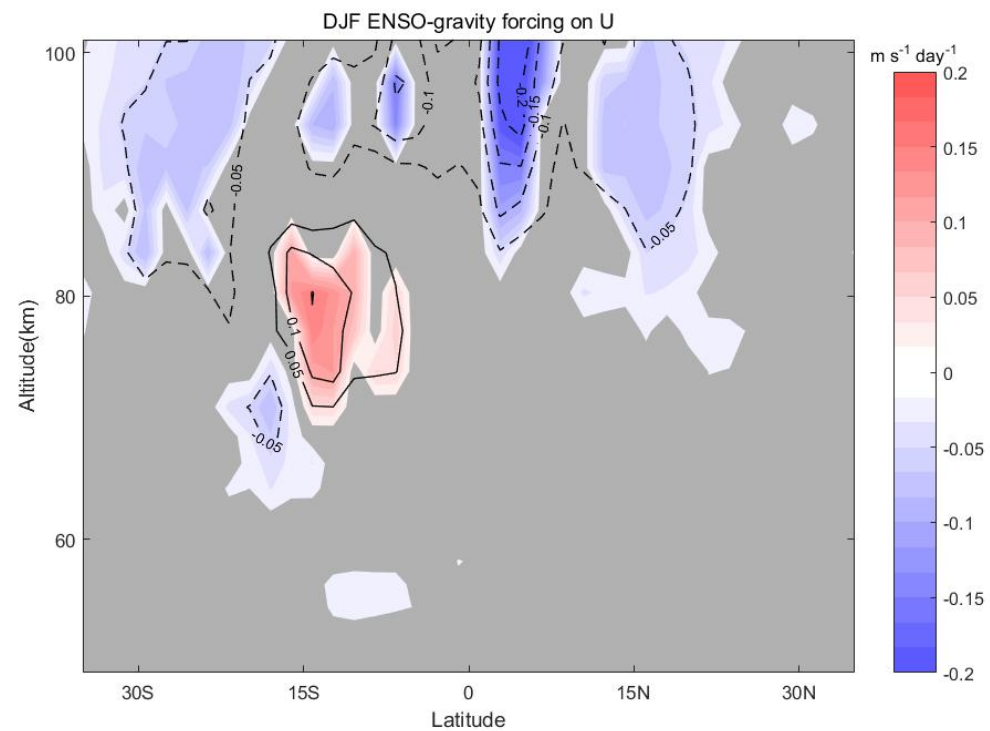


Figure 9. The linear regression coefficient of normalized Niño3.4 in the GW forcing on the amplitude of DW1-U during the 1979-2013 winters (DJF). Solid lines and red shadings denote the positive responses, while dashed lines and blue shadings denote the negative responses; the grey regions indicate where the response is insignificant at the 95% level according to the F test.